ADVANCED MATERIALS

Supporting Information

for *Adv. Mater.,* DOI: 10.1002/adma.202110085

Stimuli-Responsive Liquid-Crystal-Infused Porous Surfaces for Manipulation of Underwater Gas Bubble Transport and Adhesion

Adil Majeed Rather, Yang Xu, Yun Chang, Robert Lewis Dupont, Angana Borbora, Ufuoma Israel Kara, Jen-Chun Fang, Rajdeep Mamtani, Meng Zhang, Yuxing Yao, Solomon Adera, Xiaoping Bao, Uttam Manna,* and Xiaoguang Wang**

Supporting Information

Stimuli-Responsive Liquid Crystal-Infused Porous Surfaces for Manipulation of Underwater Gas Bubble Transport and Adhesion

Adil Majeed Rather,[¥] Yang Xu,[¥] Yun Chang,[¥] Robert Lewis Dupont, Angana Borbora, Ufuoma Israel Kara, Jen-Chun Fang, Rajdeep Mamtani, Meng Zhang, Yuxing Yao, Solomon Adera, Xiaoping Bao, Uttam Manna*, Xiaoguang Wang**

Dr. A. M. Rather, Dr. Y. Xu, R. L. Dupont, U. I. Kara, J.-C. Fang, R. Mamtani, M. Zhang, Prof. X. Wang
William G. Lowrie Department of Chemical and Biomolecular Engineering
The Ohio State University
Columbus, OH 43210, USA.
E-mail: wang.12206@osu.edu
Dr. Y. Chang, Prof. X. Bao
Davidson School of Chemical Engineering
Purdue Center for Cancer Research
Purdue University
West Lafayette, IN 47907, USA.
Email: bao61@purdue.edu
Dr. Y. Yao
Division of Chemistry and Chemical Engineering
California Institute of Technology
Pasadena, CA 91125, USA.
Prof. S. Adera
Department of Mechanical Engineering
University of Michigan
Ann Arbor, MI 48109, USA.
A. Borbora, Prof. U. Manna
Bio-Inspired Polymeric Materials Lab
Department of Chemistry
Indian Institute of Technology-Guwahati
Kamrup, Assam 781039, India.
Email: umanna@iitg.ac.in
Prof. U. Manna
Centre for Nanotechnology
Indian Institute of Technology-Guwahati
Kamrup, Assam 781039, India.
Prof. X. Wang
Sustainability Institute
The Ohio State University
Columbus, OH 43210, USA.

Table of Content **Page No**

Materials and Methods

The following liquid crystals (LCs) were purchased from Jiangsu Hecheng Advanced Materials Co., Ltd: 4'-pentyl-cyanobiphenyl (5CB), 4'-octyl-4-biphenylcarbonitrile (8CB), and 1,4-bis-[4-(3-acryloyloxypropyloxy)benzoyloxy]-2-methylbenzene (RM257). Water-insoluble dye (Oil Red O dye), hydrogen peroxide (H_2O_2, 30 wt% in H_2O), anionic surfactant sodium dodecyl sulfate (SDS), cationic surfactant dodecyltrimethylammonium bromide (DTAB), dimethyloctadecyl [3-(trimethoxysilyl) propyl]ammonium chloride (DMOAP, 42 wt% in methanol), photoinitiator 2,2-dimethoxy-2-phenylacetophenone (DMPAP), palladium acetate ($Pd(OAc)_2$), sodium borohydride ($NaBH_4$), and nitrobenzene were purchased from Sigma–Aldrich. Toluene, dichloromethane (DCM), dimethylformamide (DMF), chloroform, sodium hydroxide (NaOH), sodium bicarbonate ($NaHCO_3$), magnesium chloride ($MgCl_2$), magnesium sulphate ($MgSO_4$), sodium chloride (NaCl), calcium chloride ($CaCl_2$), azobenzene, hydrogen chloride (HCl), were purchased from Fischer Scientific. Anhydrous ethanol was purchased from Decon Labs Inc. Aluminum foil was procured from Thomas Scientific. Stainless steel sheet (60 mm × 30 mm) was obtained from the Mechanical Engineering workshop at the Ohio State University. Glass microscope slides (25 mm × 75 mm × 1 mm) were purchased from Fisher Scientific. Water used in all experiments was purified using a Milli-Q water purification system (Simplicity C9210). Unless stated otherwise, purchased chemicals were used as received without further modification or purification. Tirapazamine (TPZ) was purchased from Cayman Chemical. Calcein-AM and propidium iodide were purchased from Invitrogen.

Preparation of DMOAP-functionalized substrates

At first, all substrates were rinsed with water and ethanol and dried under a stream of nitrogen gas. Then, the cleaned substrates were placed in a 1% v/v DMOAP water solution (120 mL) for 15 min. Next, the substrates were gently washed with water and ethanol to remove unreacted DMOAP molecules. Afterward, the DMOAP-functionalized substrates were dried using nitrogen gas. Finally, the obtained DMOAP-functionalized substrates were stored in a dark room at ambient pressure and temperature to prevent the DMOAP functionalization from being damaged by light.

Preparation of LC-infused porous surfaces (LCIPS)

To make the LCIPS, we prepared a LC mixture (in toluene) containing a non-reactive LC mesogen (8CB, 90 wt%) and a reactive LC monomer (RM257, 10 wt%). DMPAP was added to the mixture as a photoinitiator at 1 wt% based on the total mass of the LC. Next, 100 µL of the homogenous LC mixture was uniformly spread across a 25 mm × 25 mm DMOAP-functionalized glass slide. Subsequently, the LC mixture-coated glass was placed under a UV

lamp (Spectroline, EA-140; 365 nm) and exposed at 2.0 mW/cm^2 for 20 min to prepare a ~160 µm-thick 8CB-swelled porous polyRM257 substrate. Finally, we spin-coated 80 µL of the same non-reactive LC mesogen (8CB) onto the 8CB-swelled polyRM257 nanoporous structure to form a LCIPS. In addition, we tested the fabrication of LCIPS on different substrates, including wood, steel, tin, cotton fabric, aluminum foil and rubber, and on different substrate shapes including serpentine, arc, Y-shaped, and curved surfaces using the same procedure. Moreover, we fabricated the azobenzene-doped LCIPS following the same protocol as reported above for LCIPS, but a mixture of azobenzene-doped 8CB (5 wt% azobenzene) was used instead of pure 8CB on the porous polyRM257 structure. The optical appearance of the 8CB surface in air and underwater with an air bubble on the surface was recorded using an Olympus BX53 microscope equipped with crossed polarizers.

Characterization of the morphology of porous polyRM257 substrates

The surface morphology of porous polyRM257 substrate was imaged using scanning electron microscopy (SEM). The porous polyRM257 substrate for SEM imaging was prepared through the photopolymerization of a mixture of 10 wt% RM257 in 8CB followed by extraction of the 8CB. The substrate was sputtered with a thin layer of gold and the imaging was performed on an FEI Quanta 200 SEM with an acceleration voltage of 5 kV at the working distance of 9 mm.

Contact angle goniometer analysis

A KRÜSS DSA 100 goniometer was used to measure contact angles (both advancing and receding) and sliding angles using a sessile drop method. Contact angles and sliding angles were measured using 10 µL air bubbles placed on the LCIPS underwater. For sliding angle measurements, we tilted the surface at a rate of 1 ^{o}/min using a built-in function on the contact angle goniometer. The angle of inclination at which the air bubble began to slide was defined as the corresponding sliding angle. In addition, the interfacial tensions were measured using a pendant drop method based on the shape of a suspended droplet. The interfacial tensions were calculated from approximately 10 measurements taken from 3 different droplets. A high-resolution camera was equipped to capture images of the droplets and air bubbles to calculate the surface and interfacial tensions using built-in software. For water–LC interfacial tension measurements, water was placed inside a quartz cell, and the LC was placed in a syringe with a needle tip held under the surface of the water. A Linkam PE120 Peltier hot stage was used to control the temperature during these measurements.

Force measurement of air bubbles on LCIPS

We performed force measurements of air bubbles with different volumes on smectic A and nematic LCIPS using a Kruss tensiometer-based microelectromechanical balance system.

Specifically, an air bubble was suspended with a metal loop connected to a microbalance, and the underlying substrate was moved upward at a constant speed of 0.6 mm/min until the substrate contacted and squeezed the air bubble. The substrate was then moved down with the same speed to detach the air bubble. During the whole measuring process, the change in the force was recorded, and the adhesion forces were obtained from the force–distance curves.

Stability and durability test of LCIPS

We performed additional experiments to investigate the stability and durability of LCIPS. In the first set of experiments, a nematic LCIPS (40 mm × 10 mm) was submerged underwater consecutively for 30 days, and the bubble transport property was examined at intervals of 5 days using a 10 μL air bubble on the LCIPS tilted at 5º. In the second set of experiments, five independent scratches were made on a nematic LCIPS using a knife. The sliding behavior of bubbles was examined on the scratched substrate by placing a 10 μL air bubble on the scratched LCIPS tilted at a 5º inclination. In the third set of experiments, we sought to examine the impact of different aqueous chemical conditions on the stability of the LCIPS. This was done by immersing both smectic A and nematic LCIPS in aqueous solutions of different chemicals. Specifically, we prepared aqueous solutions with pH ranging from 1 to 13 using concentrated HCl (6 M) and NaOH pellets. Aqueous solutions containing synthetic surfactants (1 mM DTAB or SDS) and artificial seawater [a mixture of $MgCl_2$ (0.226 g), $MgSO_4$ (0.325g), NaCl (2.673g) and $CaCl_2$ (0.112 g) in 100 mL of deionized water] were also prepared. Next, we immersed the smectic A and nematic LCIPS in the aqueous solutions and examined the stability of the LCIPS by placing a 10 μL bubble on the LCIPS tilted at a 5º inclination. Finally, we tested the nematic LCIPS in aqueous solutions of 20% ethanol (v/v), 20% acetone (v/v), and 20% glycerol (v/v) and examined the stability of the LCIPS by placing a 10 μL bubble on the LCIPS tilted at a 5º inclination.

Measurement of maximum volumes of bubbles on LCIPS

In this set of experiments, we cut the glass slides into multiple pieces with widths of 1, 2, 3, 5, 7 and 10 mm followed by rinsing with water and ethanol three times to remove any contaminants. Next, we coated these surfaces with LCIPS following the above-mentioned procedures. The obtained LCIPS-coated glass substrates were placed horizontally underwater and air bubbles with volumes of 5, 10, 15, 20, 30, 35 and 40 μL were placed on the LCIPS. The maximum adhesion force between the bubble and the LCIPS was calculated using the maximum volume of the air bubble that remained on the LCIPS. To calculate the maximum adhesion forces, we measured the base width of the bubble on the LCIPS using contact angle goniometer.

Bubble-induced locomotion of LCIPS

First, we coated LCIPS on a 20 mg piece of aluminum foil with dimensions of 30 mm × 10 mm using the above-described procedure and placed it in an aqueous solution of 100 mM $NaHCO_3$. Second, we injected an aqueous solution of HCl (1 M) over the LCIPS to generate CO_2. We investigated the bubble-induced locomotion of the LCIPS in nematic (35 ^oC) and smectic A phases (25 ^oC).

Preparation of Pd nanoparticle-decorated aluminum foil coated with LCIPS

First, a 2 cm × 1 cm, 10 mg aluminum film was treated with 1M NaOH for 2 min and was subsequently washed with water and ethanol. Next, 2 mL of a DMF solution consisting of 5 mg of $Pd(OAc)_2$ was added to the surface of the aluminum foil, and the Pd nanoparticles were formed via reduction using a 1M $NaBH_4$ aqueous solution. Finally, 0.2 cm × 0.2 cm area of the Pd nanoparticle-decorated aluminum foil was coated with LCIPS for bubble adhesion.

Bubble-induced termination in the hydrogenation of nitrobenzene using Pd nanoparticle-decorated LCIPS-coated aluminum foil

The Pd nanoparticle-decorated LCIPS-coated aluminum foil was added to a 2 mL water/ethanol solution (1:1 v/v) consisting of 1 mmol nitrobenzene. Next, 2 mmol $NaBH_4$ was added to the mixture. During the hydrogenation of nitrobenzene, the whole solution was stirred at room temperature. A 20 μL bubble was placed on the smectic A LCIPS region so that the Pd nanoparticle-decorated LCIPS-coated aluminum foil would ascend to the air–water surface to terminate the reaction. The conversion of nitrobenzene was analyzed by GC-2010 gel chromatography.

Bubble-induced origami box folding

A piece of aluminum foil with dimensions of 60 mm × 60 mm was cut into an open structure with four 20 mm × 20 mm arms. Next, LCIPS was coated on the edge of all four arms of the aluminum foil. Afterward, the aluminum foil was placed underwater at 25 ^oC, and the center of the aluminum foil was adhered to the bottom of the tank. Finally, we placed two 20 μL air bubbles consecutively on each arm to activate the process of the origami box folding. The maximum mass that a 20 μL air bubble can lift up was calculated to be ~ 31 mg, and the mass of one arm was 60 mg.

Patterned LCIPS for guided oxygen transport

A piece of aluminum foil with dimensions of 50 mm × 40 mm was cut into a patterned LCIPS with two 20 mm × 5 mm branches on each side. We used LCs with different phase transition temperatures (8CB and 5CB at 25 ^oC for designing smectic A and nematic regions on the LCIPS) to pattern the LCIPS surfaces to selectively pin and slide air bubbles underwater.

Specifically, we coated smectic A LCIPS on two branches and nematic LCIPS on the other branches (at 25 °C) using 8CB and 5CB. Then, a piece of potato (10 mm × 10 mm × 10 mm) was placed at the bottom of the patterned LCIPS underwater. Finally, H_2O_2 (30 wt% in H_2O) was injected onto the potato piece to generate oxygen bubbles (Figure S18).

Design of arc-shaped gas bubble gating system

First, a flat stainless-steel substrate was cleaned by rinsing with water and ethanol three times. Next, we coated LCIPS on the steel substrate before bending the steel substrate manually into an arc shape and immersing the LCIPS-coated steel substrate under water. In our experiments, we placed 15 μL bubbles on both sides of the arc shape.

Sorting and sensing of volatile organic compounds (VOCs) in air bubbles

In this experiment, we sought to use LCIPS to sort and sense VOC-containing air bubbles from pure air bubbles. Specifically, we designed a prototype device using an acrylic box, a LCIPS-coated glass substrate and acrylic barrier. The LCIPS was immersed under water in the box at a 10° inclination. Next, we generated toluene-contaminated air bubbles by heating the toluene solvent above its boiling point and collected using a micro syringe. We then placed both pure air bubbles and toluene-contaminated air bubbles on the LCIPS using a micro syringe.

Cell culture used in this study

Human glioblastoma cell line (U87MG) was cultured in Eagle's Minimum Essential Medium (MEM) (containing 10% fetal bovine serum, 100 units/mL penicillin and 100 mg/mL streptomycin). Human breast cancer cell line (MDA-MB-231) was cultured in an L15 medium containing 2 mM glutamine, 15% fetal bovine serum, and 100 units/mL penicillin and 100 mg/mL streptomycin. Human lung cancer cell line (A549) was cultured in Ham's F12K containing 2 mM glutamine, 10% fetal bovine serum, and 100 units/mL penicillin and 100 mg/mL streptomycin. These three cell lines were incubated at 37 °C in a humidified 5% CO_2 atmosphere. The accessible inner volume of the cell incubator is approximately 15 mL, and the nitrogen bubble flow rate by the nematic LCIPS-based bubble gating system is approximately 600 μL/min.

Reverse transcription PCR (RT-PCR) analysis

For RT-PCR analysis, 4×10^4 cells were plated in a well of a 24-multiwell plate and cultured overnight. Attached tumor cells were then treated with the LC bubble gating system for 24 hours and rinsed with cold PBS buffer once and lysed in 500 μL of TRIzol™ reagent (Invitrogen). Total RNA was then prepared with Direct-zol RNA miniprep kit (Zymo) with in-column DNase treatment following the manufacturer's instructions. cDNA was reverse-transcribed from 1 μg RNA with ProtoScript First Strand cDNA Synthesis Kit (NEB) and used

for RT-PCR with GoTaq Green Master Mix (Promega). GADPH was used as an endogenous housekeeping control, and the primer pairs for targeted genes are listed below:

GAPDH (forward): GTGGACCTGACCTGCCGTCT;

GAPDH (reverse): GGAGGAGTGGGTGTCGCTGT;

HIF1α (forward): GGACAAGTCACCACAGGACA;

HIF1α (reverse): TCAACCGGTTTAAGGACACA.

Cytotoxicity measurements

1×10^4 cells in 100 μL of culture medium were plated in each well of a 96-multiwell plate overnight. For tumor cells without the LC-based bubble system, the culture medium was removed and the cells were treated with 100 μL of a culture medium containing 20 μg/mL of TPZ for 24 hours. Cells under the LC bubble system were cultured using this system for 24 hours after the culture medium change. Treated tumor cells were stained with 100 μL of the mixture of 1 μM Calcein-AM (Invitrogen) and 1 μM propidium iodide for 30 minutes. After washing three times with PBS buffer, tumor cells were visualized and imaged in the Leica DMi-8 fluorescent microscope.

Results

Morphology of the porous polyRM257 structure

As shown in Figure S1, the surface morphology of the polyRM257 substrate was analyzed using SEM imaging. A nanoporous network was observed, which is essential for the stability of the lubricant layer and the creation of a stable lubricant infused slippery surface.

Stability criteria of LCIPS against dewetting by water

In this section, we sought to provide a theoretical observation on the stability of the LCIPS against dewetting by water. Aizenberg and coworkers have reported the energy criteria to stabilize an isotropic lubricant film against dewetting by water droplets.[1] Accordingly, the total interfacial energy (ΔE_1) of the porous polyRM257 substrate wetted by water (E_A) needs to be higher than that wetted by the LC with (E_1) and without (E_2) water droplets on the surface for there to be no dewetting of the porous polyRM257 substrate, which can be written as:

$$\Delta E_1 = E_A - E_1 = r\,(\gamma_{LC}\cos\theta_{LC} - \gamma_w\cos\theta_w) - \gamma_{w-LC} > 0 \quad \text{(S1)}$$

$$\Delta E_2 = E_A - E_2 = r\,(\gamma_{LC}\cos\theta_{LC} - \gamma_w\cos\theta_w) + \gamma_w - \gamma_{LC} > 0 \quad \text{(S2)}$$

in which r is the roughness factor (defined as the ratio of true surface area of the porous polyRM257 surface to the projected surface area), γ_{w-LC} is the interfacial tension between water and the LC, and γ_w and γ_{LC} represents the surface tension of water and the LC, respectively. θ_w and θ_{LC} are the equilibrium contact angles of water and the LC on the solid surface, respectively. We measured the equilibrium contact angles and surface tensions of water and LC on the LCIPS, as summarized in Table S1. After substituting the values from Table S1 into Equations S1 and S2, we calculated ΔE_1 = + 7.0 mJ/m^2 and ΔE_2 = + 65.9 mJ/m^2. These results suggest that the LC layer is stable on the porous polyRM257 substrate, preventing water-induced dewetting.

LC wrapping layer at LC–water interface on air bubble

In this section, we provide theoretical reasoning on the presence of a wrapping layer of LC around an air bubble on the LCIPS. We calculated the spreading coefficient (S) of nematic 8CB at the air–water interface, which can be calculated as:[2,3]

$$S = \gamma_w - (\gamma_{w-LC} + \gamma_{LC}) \quad \text{(S3)}$$

in which γ_w is the surface tension of water (72.8 mN/m), γ_{w-LC} is the interfacial tension of water–8CB (19.5 mN/m), and γ_{LC} is the surface tension of 8CB (33.5 mN/m). A wrapping layer is formed when $S > 0$.[4] Using the above values, we calculated S = +19.8 mN/m, suggesting the presence of a nematic 8CB wrapping layer around the air bubble on a nematic LCIPS.

Optical appearance of LCIPS with bubbles underwater

The optical appearance of an LCIPS under air bubbles was observed using an optical microscope. As shown in Figure 1b, in the nematic phase (35 ºC), the air bubble (2 µL) changes

the optical appearance of LCIPS underwater from bright to dark, suggesting a change in the LC alignment from planar (at the water–LC interface) to homeotropic (at the air–LC interface). The homeotropic alignment of LC mesogens was further confirmed with the conoscopic image as shown in the inset of Figure 1b. In the smectic A phase (25 ºC), a focal conic domain pattern was observed when the LCIPS was placed underwater (Figure S2a). Similar to the nematic phase, a dark appearance was observed under the air bubble (2 µL), as shown in Figure S2a. According to previous studies, focal conic domain structures form under antagonistic surface anchoring conditions (e.g., planar on one surface and perpendicular on the other).[5-8] In our experiments, 8CB mesogens align perpendicular to the bottom substrate and parallel to the water, resulting in the formation of focal conic domain structures under water, as illustrated in Figure S2b.

LC mesophase-dependent contact angle hysteresis

We measured the apparent contact angles of air bubbles on LCIPS according to the previous report by McHale et al.[9] The apparent contact angle of air bubbles on an LCIPS remains almost constant (~ 68º) in both the nematic and smectic A phases (from 25 ºC to 40 ºC), as shown in Figure S3. It is well known that the static friction force of air bubbles sliding on a surface is governed by the contact line pinning,[10,11] which is caused by contact angle hysteresis:

$$\Delta\rho g V \sin\alpha = 2r\,(\gamma_{w-LC} + \gamma_{v-LC})\cdot(\cos\theta_{Rec} - \cos\theta_{Adv}) \quad \text{(S4)}$$

$$\text{or } (\cos\theta_{Rec} - \cos\theta_{Adv}) = \Delta\rho g V \sin\alpha \,/\, 2r\,(\gamma_{w-LC} + \gamma_{v-LC}) \quad \text{(S5)}$$

where $\Delta\rho$ is the mass density difference between air and water, g is the gravitational acceleration, V is the volume of the air bubble on the LCIPS, r is the base radius of the air bubble on the LCIPS, and θ_{Adv} and θ_{Rec} are the advancing and receding contact angles of the air bubble, respectively. We comment here that Equation S4 is the same as Equation 1 of the main text. We also note here that the use of '$\gamma_{w-LC} + \gamma_{v-LC}$' instead of the surface tension of water (γ_{v-w}) is because of the formation of a LC wrapping layer around the air bubble on the LCIPS. After substituting the values in Equation S5, we can calculate the contact angle hysteresis (defined as '$\cos\theta_{Rec} - \cos\theta_{Adv}$' for simplicity) of the air bubble on the LCIPS. The contact angle hysteresis of a 10 µL air bubble was calculated to decrease from ~ 0.29 in the smectic A phase (25 ºC) to ~ 0.03 in the nematic phase (35 ºC), as shown in Figure S5. We reason here that with an increase in the temperature, 8CB transitions from the smectic A phase (one-dimensional positional order) to the nematic phase (no positional order). This decrease in mesogenic positional order leads to a decrease in the surface roughness of the LCIPS, which in turn decreases the contact angle hysteresis of the air bubble on the LCIPS. This result leads us to conclude that the

positional order of the LC significantly impacts the static friction force acting on air bubbles on the LCIPS.

Stimuli-responsive manipulation of air bubbles underwater

The above results indicate that the LC mesophase-dependent positional order of the LC prominently impacts the static friction of air bubbles on a LCIPS. In this section, we explored the possibility of using external stimuli to switch the LC mesophase to manipulate the mobility of underwater air bubbles on a LCIPS. First, we sought to use UV light to activate the sliding of air bubbles on the LCIPS. Specifically, we doped 8CB with 5 wt% azobenzene. As shown in Figure S6b and Supplementary Movie 1, when a 10 μL air bubble was placed on the azobenzene-doped LCIPS in the smectic A phase (25 ^{o}C) that was inclined by 10^{o}, the bubble remained strongly pinned without any movement for six hours. However, upon exposure to UV light (365 nm wavelength), the induced *trans–cis* isomerization of azobenzene prompted a smectic A to nematic phase transition of 8CB (Figure S8b), causing the air bubble to slide easily across the nematic 8CB surface. In contrast, air bubbles remained immobile upon exposure to UV on smectic A LCIPS without doping with azobenzene molecules, as shown in Figure S6c. Moreover, the transport of air bubbles on LCIPS can be reversibly activated and deactivated without any measurable perturbations via the UV-induced LC phase transition when the UV light was turned on and off alternatively, as shown in Figure S7. Next, we sought to activate the sliding of bubbles on an LCIPS using chemical stimuli. As shown in Figure S6d and Supplementary Movie 1, the LCIPS was placed underwater in the smectic A phase (25 ^{o}C) with an inclination of 30^{o}. When a 20 μL toluene vapor bubble was placed on the LCIPS, the toluene vapor gradually diffused into the LCIPS and triggered a smectic A to nematic phase transition of the 8CB, resulting in the sliding of the toluene vapor bubble on the LCIPS. In addition, this functionality is generalizable to other common organic chemical vapors including chloroform and dichloromethane. Furthermore, we performed polarized light microscopy imaging to confirm the LC phase transition induced by UV and toluene as shown in Figure S8. These results show that this LCIPS system offers a multitude of possibilities, for example, the guided transport of hazardous gases underwater and smart bubble and drug delivery.

Physical and chemical durability of LCIPS and generalizability for different substrates

Here we sought to investigate the physical and chemical robustness of LCIPS and the generalizability of the approach to design LCIPS on a variety of substrates with different shapes and chemical structures. As shown in Figure S9, LCIPS retained their slipperiness towards air bubbles after multiple physical damages and after constant submersion underwater for 30 days. Moreover, air bubbles can slide smoothly on nematic LCIPS without severe pinning in different

harsh aqueous chemical conditions including extremes of pH (1–13), surfactant-contaminated water (SDS and DTAB), artificial seawater, and different aqueous solutions containing 20 v/v % of ethanol, glycerol, or acetone, as shown in Figures S10 and S11. In addition, air bubbles remained pinned on smectic A LCIPS in the above mentioned different harsh chemical conditions and even under shaking and vibration, as shown in Figure S12, S13 and Movie S2. Finally, we demonstrate that LCIPS fabrication is generalizable to a variety of substrates such as rubber, cotton fabric, wood, aluminum foil, steel, and tin, as well as substrates in various shapes, including serpentine, arch shape, Y-shape, and a curved glass vial as shown in Figure 2e and Figure S14. Overall, these results demonstrate the outstanding stability and generalizability of our LCIPS design.

LC mesophase-dependent bubble adhesion on LCIPS

It is well known that adhesion force between the surface and the air bubble stabilizes the air bubble on the LCIPS against buoyancy. The maximum adhesion force between the bubble and the LCIPS can be calculated using the maximum volume of air bubbles (Figure S15) that remain attached to the surface (V_{critical}):

$$F_{\text{adhesion}} = \Delta\rho g V_{\text{critical}} \tag{S6}$$

We prepared LCIPS-coated substrates with different widths to investigate the effect of substrate dimensions on the maximum adhesion force between the bubble and the substrate. As shown in Figure S16, the maximum adhesion force increases with an increase in the substrate width and remains constant above a threshold substrate width, i.e., 5.6 mm and 4.7 mm for the smectic A and nematic phases, respectively. The respective maximum adhesion force is calculated to be ~ 340 µN and ~ 190 µN on LCIPS in the smectic A phase and nematic phase, respectively.

Calculation of receding contact angles of air bubbles on LCIPS

To provide insights into the adhesion between air bubbles and the LCIPS, the maximum adhesion force can be balanced by the pinning force of the receding contact lines of the air bubbles:

$$\Delta\rho g V_{\text{critical}} = 2\pi r\,(\gamma_{\text{w–LC}} + \gamma_{\text{v–LC}})\sin\theta_{\text{Rec}} \tag{S7}$$

$$\text{or } \sin\theta_{\text{Rec}} = \Delta\rho g V_{\text{critical}} / 2\pi r\,(\gamma_{\text{w–LC}} + \gamma_{\text{v–LC}}) \tag{S8}$$

We note here that Equation S7 is the same as Equation 2 of the main text. To estimate the θ_{Rec}, we measured the base radius of the air bubbles as a function of bubble volume. As shown in Figure S15, the base width for V_{critical} was extracted by extrapolating the data to 40 µL and 25 µL for the smectic A and nematic phases, respectively. After substituting the values in Equation S8, the θ_{Rec} of bubbles on smectic A and nematic LCIPS was calculated to be ~ 155° and ~ 161°, respectively, as shown in Figure S16c. These results, combined with our experimental

observations (different θ_{Rec} and r of air bubbles on LCIPS) lead us to propose that the high surface roughness of smectic A 8CB causes more severe pinning of air bubbles at its surface relative to those observed in the nematic phase, resulting in a higher adhesion force of air bubbles on smectic A LCIPS.

Bubble-regulated locomotion of LCIPS and origami box folding

Inspired by the depth control of cyanobacteria through buoyancy regulation, here we sought to control the depth of LCIPS underwater through manipulation of bubble adhesion on the LCIPS. Specifically, we immersed a 55 mg LCIPS-coated aluminum foil with dimensions of 30 mm × 10 mm in an aqueous solution of $NaHCO_3$ (100 mM). We then injected HCl (1 M) into the solution to generate CO_2 bubble above the surface of LCIPS. In hot water (35 ^oC; nematic phase), the CO_2 bubbles generated on the LCIPS could not remain attached to the LCIPS, causing no measurable movement to the LCIPS, as shown in Figure S17 and Supplementary Movie S3. However, in cold water (25 ^oC; smectic A phase), the formed CO_2 bubbles attached to the center of the LCIPS substrate consequently lifting it up owing to the strong adhesion between the bubble and the LCIPS (Supplementary Movie S3). Moreover, the position of the bubble at the surface of the LCIPS determines the locomotion of the LCIPS. For instance, when the bubble was generated at the edge of LCIPS, the generated bubble tilted the LCIPS substrate up, as shown in Figure 3f, g and Supplementary Movie 3. In addition, we placed two 20 µL gas bubbles on each arm of an open structure to fold in an origami manner. The maximum mass that a 20 µL air bubble can lift up was calculated to be ~ 31 mg, and the mass of one arm was 60 mg.

Sorting and sensing of volatile organic compounds (VOCs)

VOCs are considered one of the most prevalent environmental pollutants and are a direct threat to human health owing to their high toxicity.[12] Exposure to even low concentrations of VOC vapors can cause a variety of severe diseases by disrupting the nervous system and hampering cellular activity.[13] Hence, the detection of VOC vapors with superior sensitivity is becoming increasingly important. To address this environmental challenge, we have designed a prototype device that can not only sense VOCs in air bubbles but, more importantly, sort the air bubbles based on the presence of VOCs. As shown in Figure 4b,c, when a pure air bubble was introduced from the inlet of the device, the bubble detached from the smectic A LCIPS and was released to the outlet of compartment 1. In contrast, when an air bubble contaminated by a VOC was introduced, the VOC locally triggered the smectic A–nematic phase transition, resulting in the sliding of the VOC-containing air bubble on the tilted LCIPS and a subsequent detachment from the end of the LCIPS into the outlet of compartment 2. Furthermore, this prototype device

can efficiently sense and sort air bubbles based on VOC contamination for more than 600 successive bubbles, as shown in Figure 4b, and were shown to sense VOC concentrations as low as ~ 7 ppm. More importantly, this prototype is generalizable to other common organic chemical vapors including chloroform and dichloromethane containing VOCs.

Table S1. Interfacial tension and contact angle measurements of water and 8CB at porous substrates. $n = 3$ for the means and standard deviations.

θ_w (^{o})	84.5 ± 1.7
θ_{LC} (^{o})	0
γ_w (mN/m)	72.8 ± 1.6
$\gamma_{w–LC}$ (mN/m)	19.5 ± 1.1
γ_{LC} (mN/m)	33.4 ± 1.8

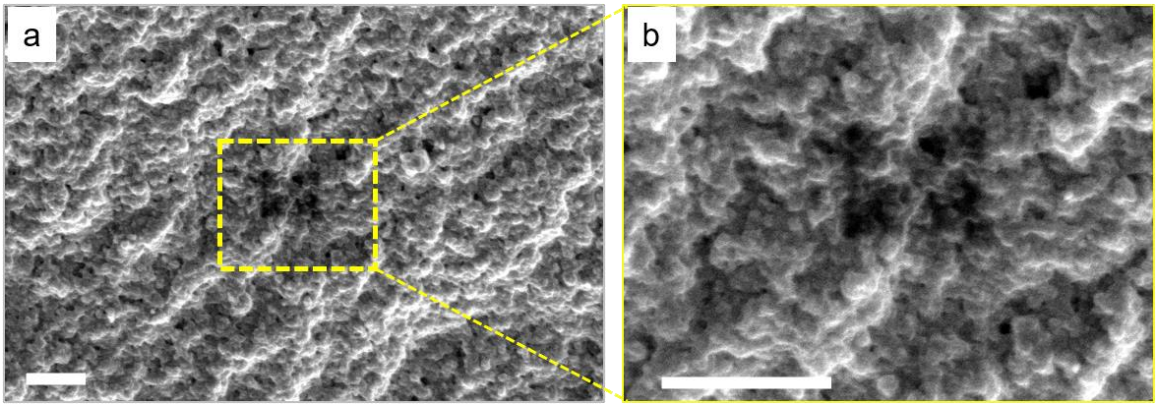

Figure S1. Scanning electron microscopy (SEM) characterization of the porous polyRM257 structure. a, b) SEM images of polyRM257 porous structure. The porous polyRM257 substrate was synthesized by photopolymerizing a mixture of 10 wt% RM257 in 8CB followed by extraction of the nonreactive mesogens (8CB) using ethanol and subsequent drying at 70 ºC. Scale bars, 5 µm.

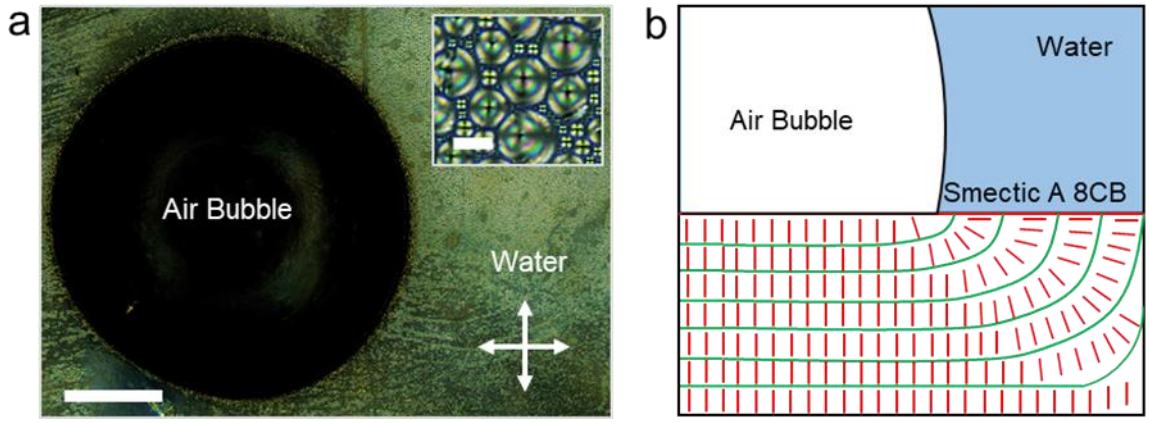

Figure S2. Orientational ordering of LCs in smectic A LCIPS. (a) Representative polarized light micrograph and (b) corresponding schematic illustration of the LC ordering of an underwater smectic A LCIPS with a 2 µL air bubble on the surface. The air bubble changes the orientation of the LC from planar to perpendicular, as seen in the transition from bright to dark. The inset in (a) shows the focal conic domain structure of smectic A 8CB underwater. Scale bars, 500 µm and 20 µm (inset). The crossed double-headed arrows in (a) indicate the orientations of the crossed polarizers. The temperature of the bulk water was 25 ^{o}C (smectic A phase). Green curves and short red lines in (b) indicate the lamellar layer structure and individual 8CB ordering, respectively.

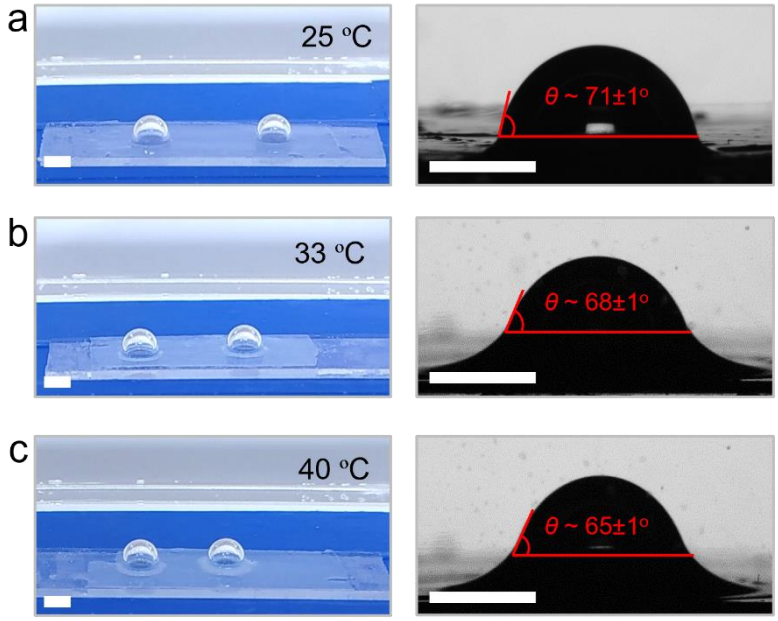

Figure S3. Wetting of air bubbles on LCIPS. a-c) Photographs and contact angle micrographs of air bubbles (10 µL) on LCIPS at different temperatures, including 25 ºC (a), 30 ºC (b) and 40 ºC (c). Apparent contact angles of air bubbles on LCIPS are listed in the contact angle micrographs. Scale bars, 2 mm.

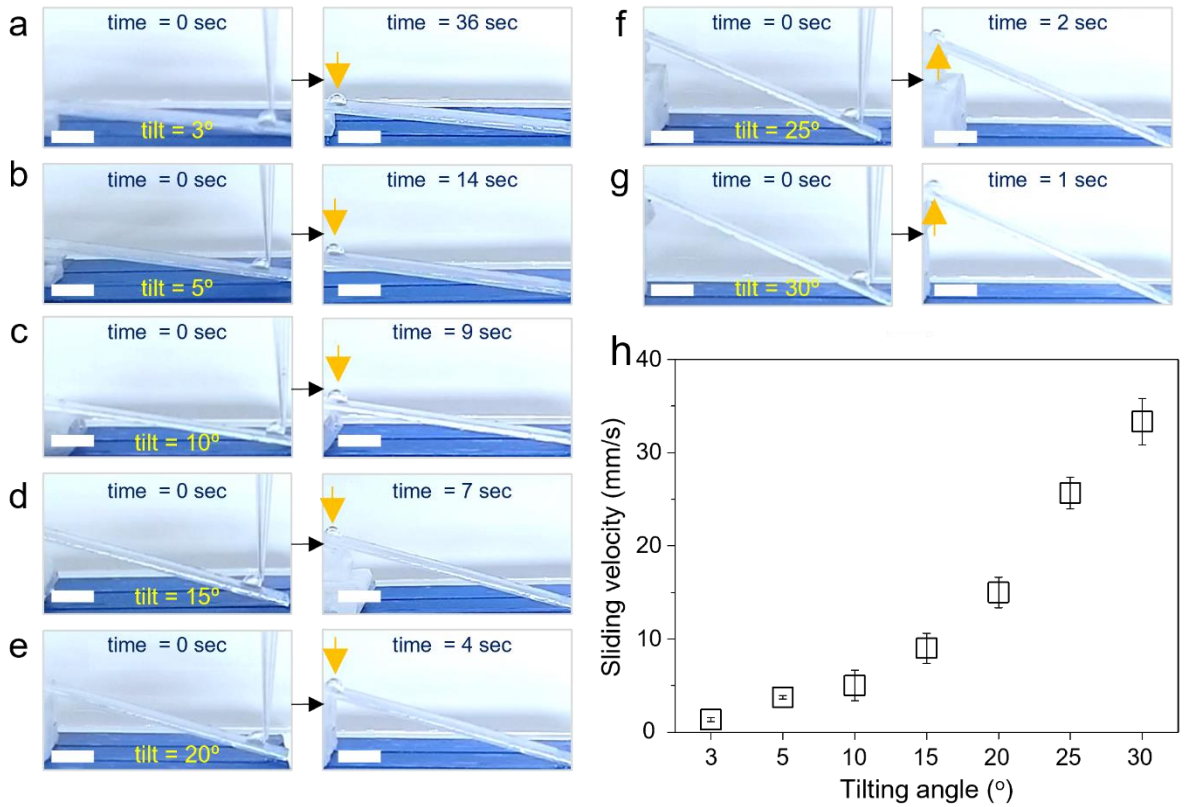

Figure S4. Sliding of air bubbles on nematic LCIPS. a-g) Photographs of air bubble sliding on nematic LCIPS placed at different tilting angles: 3º (a), 5º (b), 10º (c), 15º (d), 20º (e), 25º (f) and 30º (g). Scale bars, 5 mm. h) Sliding velocity of air bubbles on LCIPS as a function of sliding angle. The volume of the air bubble was 10 µL. The temperature of the bulk water was 35 ºC (nematic phase). Yellow arrows indicate the position of the air bubbles on the LCIPS. *n* = 3 for the means and standard deviations.

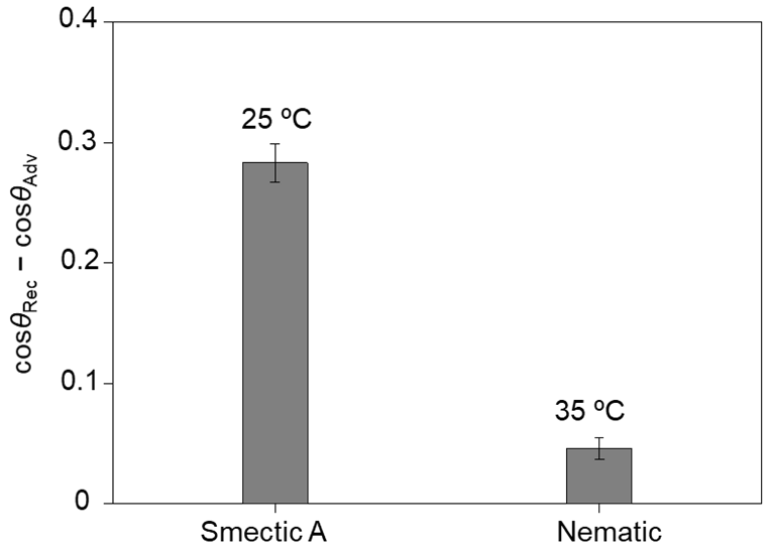

Figure S5. LC mesophase-dependent contact angle hysteresis. Calculated contact angle hysteresis (using Equation 1 of the main text) of air bubble sliding on LCIPS as a function of LC mesophases. The volume of the air bubble was 10 μL. n = 3 for the means and standard deviations.

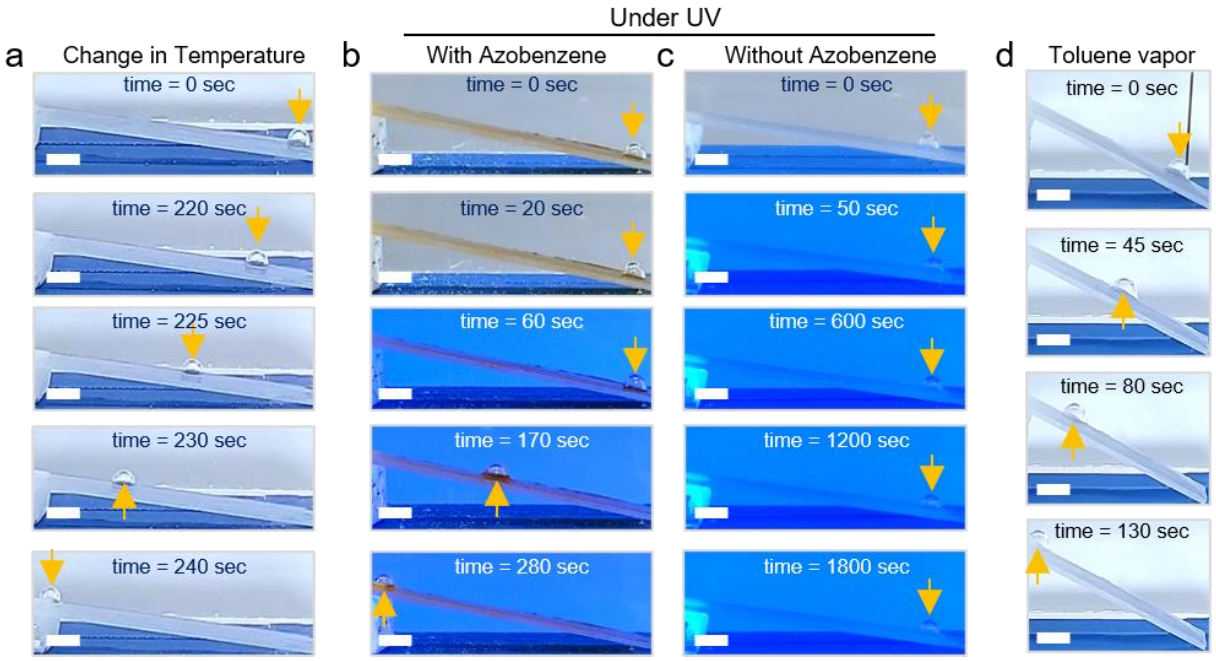

Figure S6. Manipulation of underwater air bubble sliding on LCIPS through the reversible switching of LC mesophases using external stimuli. a) Photographs of the activated sliding of air bubble on LCIPS via heating. b, c) Photographs of air bubble sliding on LCIPS with (b) and without (c) azobenzene doping upon UV exposure. The composition of azobenzene was 5 wt% based on the mass of 8CB. The UV source had a wavelength of 365 nm. d) Photographs of a toluene vapor bubble sliding on an LCIPS. In all these experiments, LCIPS were initially placed in water at 25 ºC (smectic A phase). The tilting angle was 5º in (a), 10º in (b, c) and 30º in (d). Yellow arrows indicate the position of the bubbles on the LCIPS. The bubble volume was 10 µL in (a, b, c) and 20 µL in (d). Scale bars, 5 mm.

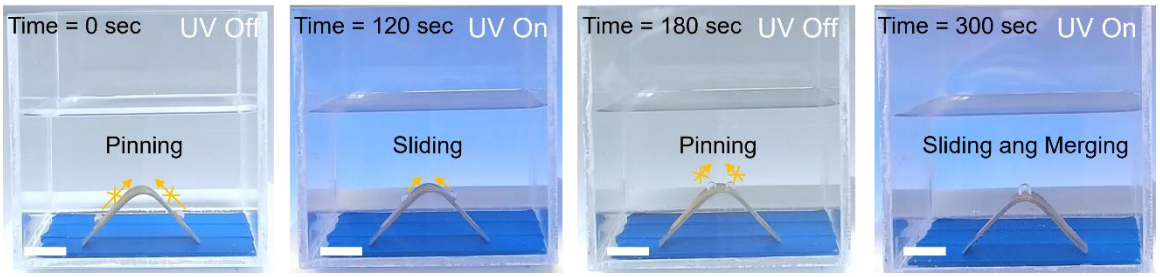

Figure S7. Reversible pinning and sliding of air bubbles on LCIPS through the reversible switching of LC mesophases using UV light. The volume of the air bubble was 10 μL. Scale bars, 5 mm.

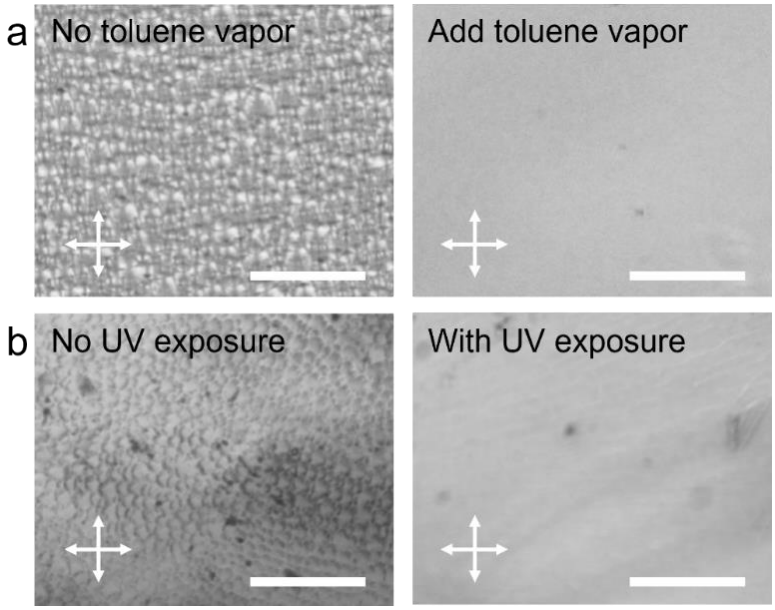

Figure S8. Polarized light micrographs showing a smectic A to nematic phase transition caused by (a) toluene or (b) UV (365 nm) exposure. The crossed double-headed arrows indicate the orientations of the crossed polarizers. Scale bars, 50 μm.

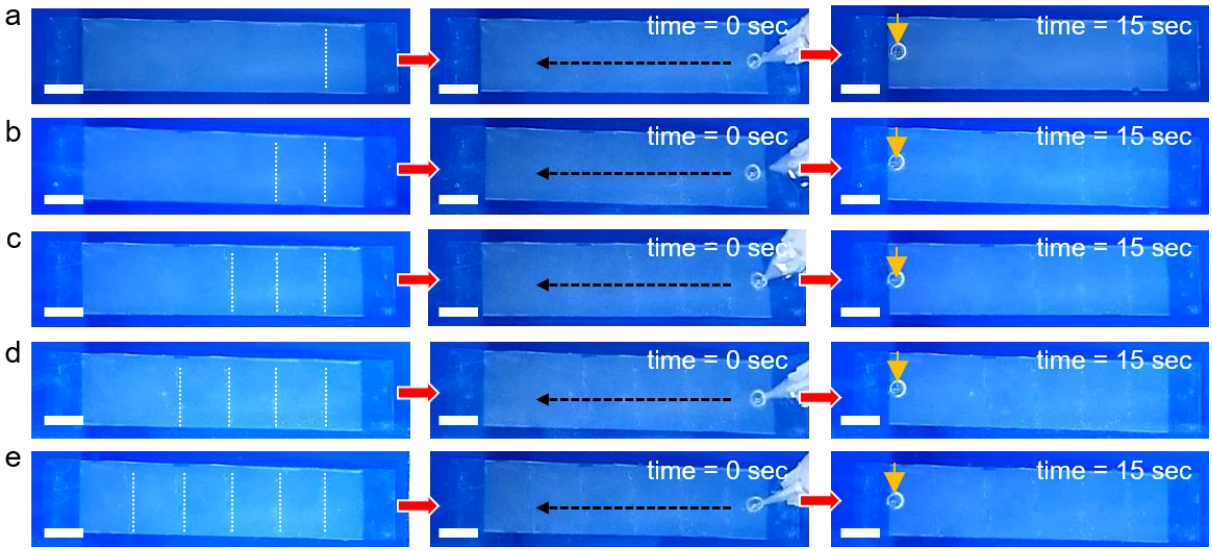

Figure S9. Physical durability of LCIPS. a-e) Photographs (top view) of an air bubble sliding on nematic LCIPS with knife scratches. White dashed lines indicate the position of the knife scratches made on the LCIPS. Black dashed arrows indicate the direction of the air bubble sliding. Yellow arrows indicate the position of the air bubbles on the LCIPS. The air bubble volume was 10 µL. The tilting angle of the LCIPS was 5º. The temperature of the bulk water was 35 ºC (nematic phase). Scale bars, 5 mm.

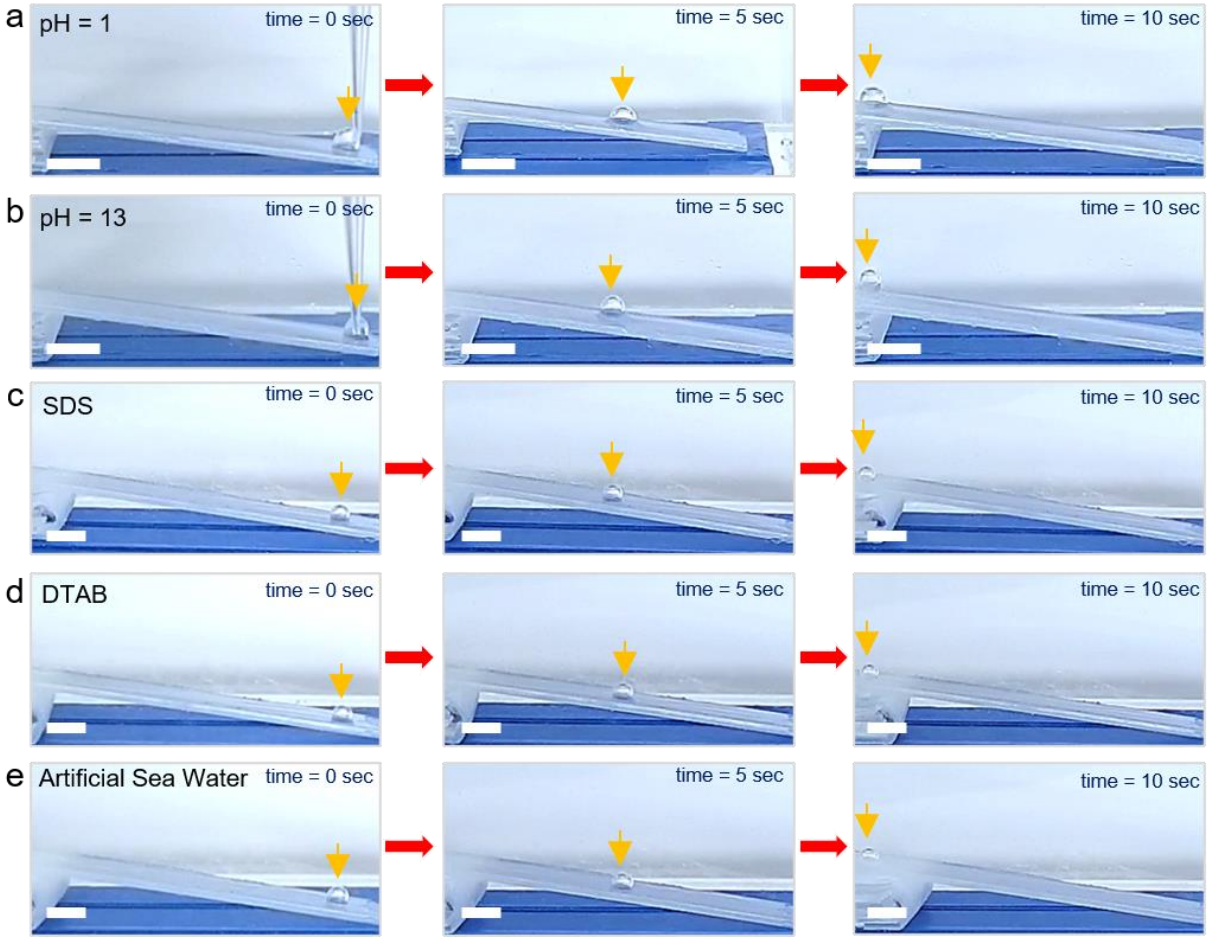

Figure S10. Chemical stability of LCIPS. a-e) Photographs of the sliding of air bubbles on nematic LCIPS in different harsh aqueous solutions: pH 1 (a), pH 13 (b), 1 mM SDS (c), 1 mM DTAB (d), and artificial seawater (e). The artificial seawater was a mixture of $MgCl_2$, $MgSO_4$, NaCl, and $CaCl_2$ in deionized water. All these LCIPS were tilted at 5º and the air bubble volume was 10 µL. The temperature of bulk water was 35 ^{o}C (nematic phase). Yellow arrows indicate the position of the air bubbles on the LCIPS. Scale bars, 5 mm.

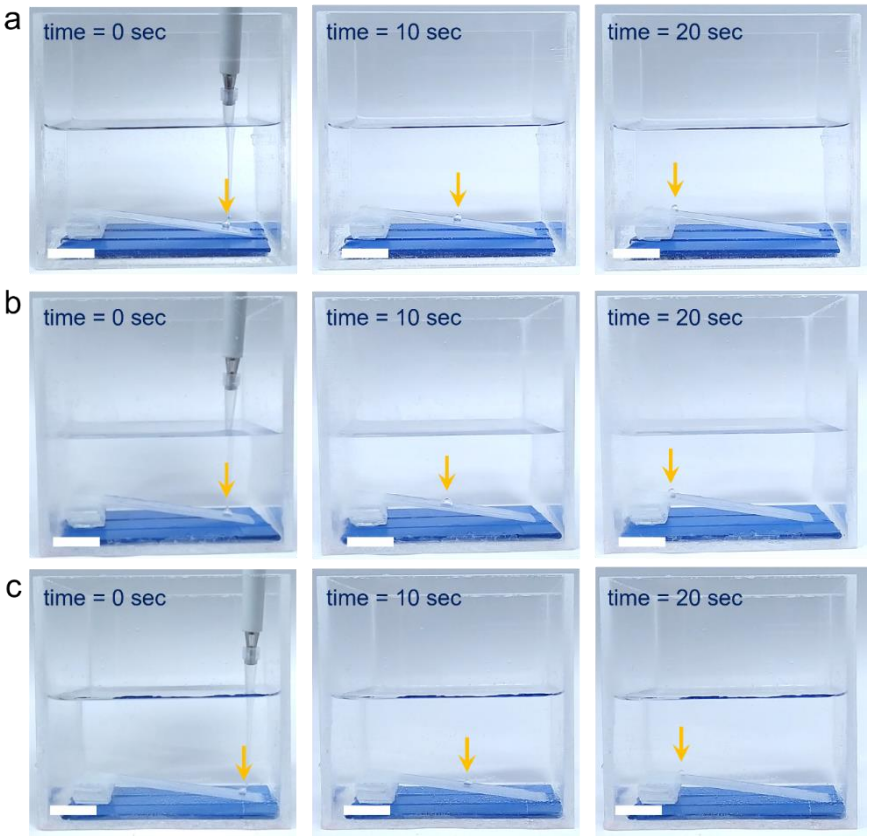

Figure S11. Bubble manipulation in water/organic solvent mixture. a-c) Sliding of an air bubble in different water/organic solvent mixtures including 20 % v/v ethanol (a), 20 % v/v glycerol (b) and 20 % v/v acetone (c). The volume of the air bubble was 10 µL. Yellow arrows indicate the position of the air bubbles on the LCIPS. Scale bars, 5 mm.

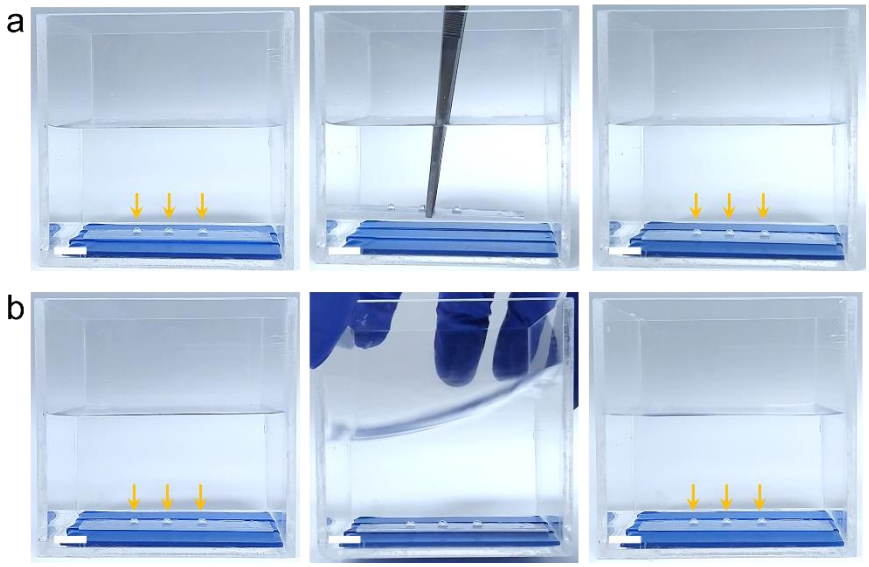

Figure S12. Stability of underwater gas bubbles on smectic A LCIPS under shaking or vibration. a, b) Air bubbles remained pinned on smectic A LCIPS under the random movement of the substrate (a) or random shaking or vibration (b). The volume of the air bubble was 10 μL. Yellow arrows indicate the position of the air bubbles on the LCIPS. Scale bars, 5 mm.

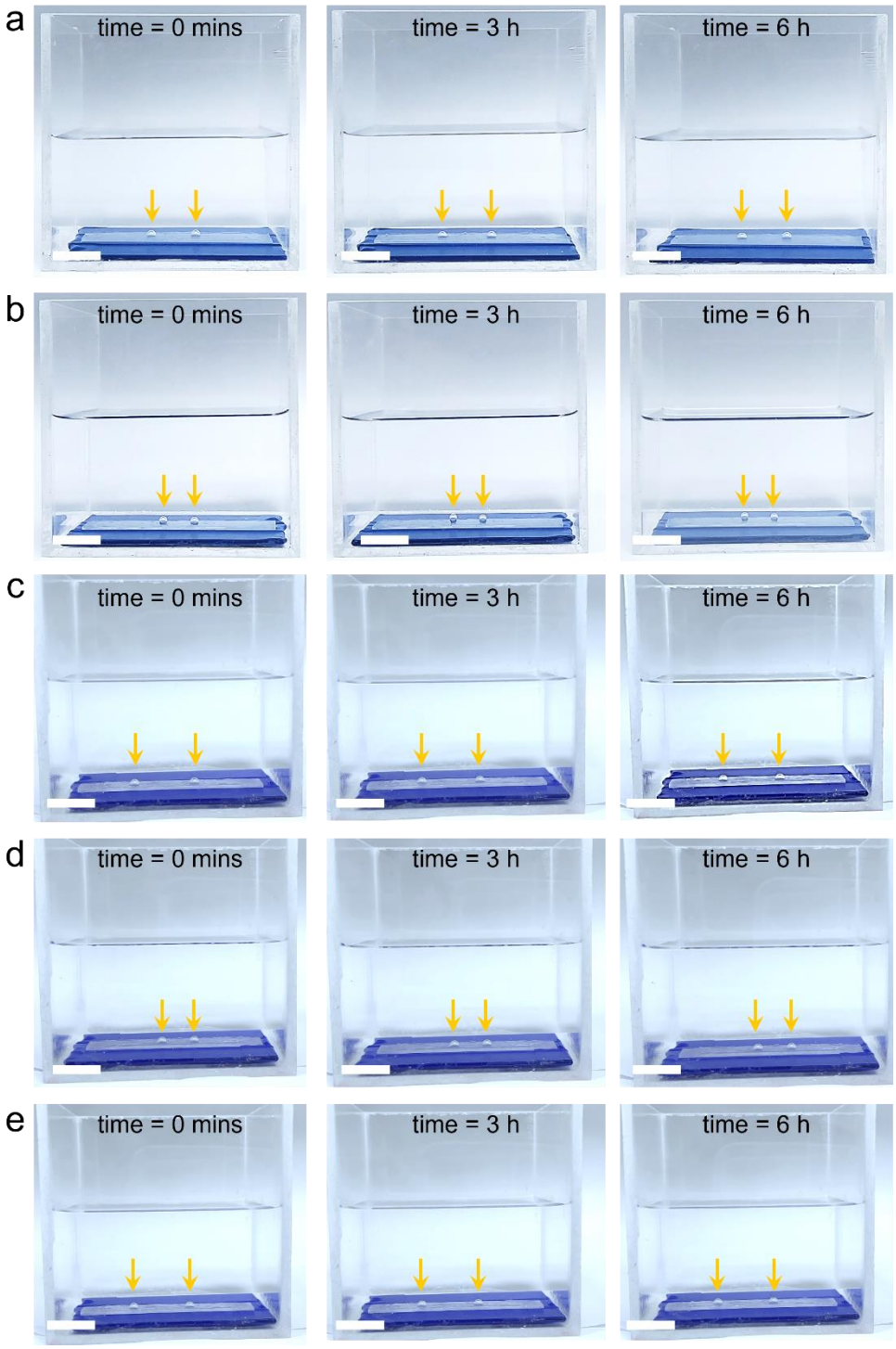

Figure S13. Stability of underwater gas bubbles on smectic A LCIPS in different chemical conditions. a-e) Stability of underwater gas bubbles on smectic A LCIPS in different aqueous conditions: pH 1 (a), pH 13 (b), artificial seawater (c), 1 mM DTAB (d) and 1 mM SDS (e). The gas bubbles remained pinned on the smectic A LCIPS in all of these chemical conditions. The volume of the air bubble was 10 µL. Yellow arrows indicate the position of the air bubbles on the LCIPS. Scale bars, 5 mm.

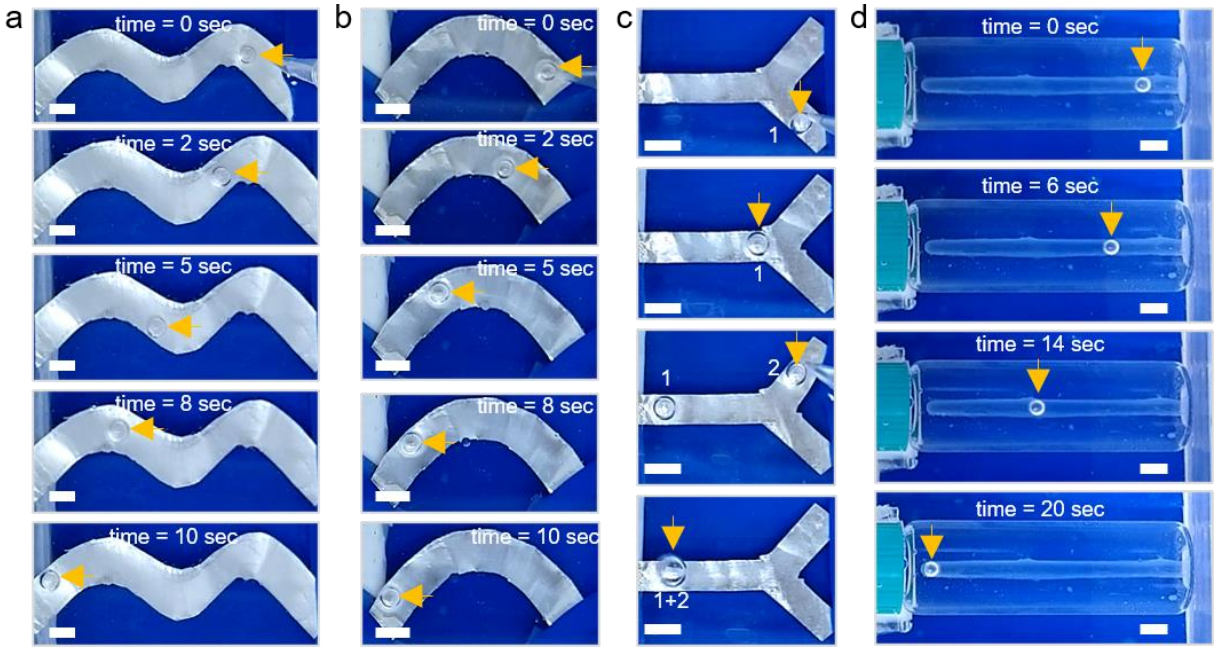

Figure S14. Directed transport of bubbles on various shapes of LCIPS. a-c) Photographs (top view) of air bubbles on a nematic LCIPS coated on aluminum substrates in serpentine (a), arc shape (b), and Y-shape (c). d) Photographs of air bubble sliding on LCIPS coated on a curved surface. The diameter of the cross-section area of the vial was 10 mm. All surfaces were placed at a tilting angle of ~5º and the volume of the air bubble was 10 µL. Yellow arrows indicate the position of the bubble on the LCIPS. Scale bars, 5 mm.

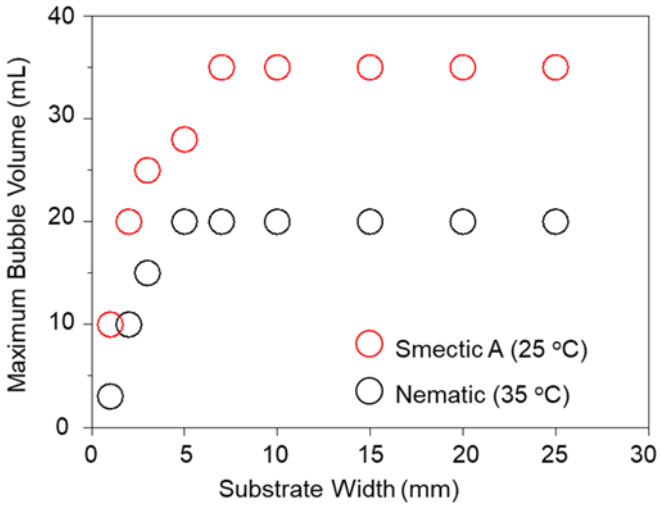

Figure S15. Maximum air bubble volume remaining attached to LCIPS as a function of the substrate width.

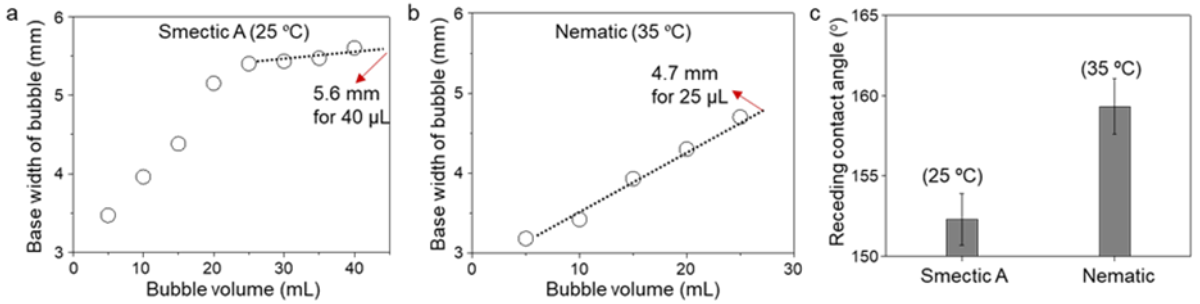

Figure S16. Estimation of the receding contact angles of air bubbles on LCIPS. a, b) Base width (diameter) of air bubbles with different volumes on LCIPS in smectic A (a) and nematic (b) phase. The base width was measured using a contact angle goniometer. The volume of the air bubbles was up to 35 µL and 20 µL for the smectic A and nematic phase, respectively. The base width for $V_{critical}$ (40 µL and 25 µL for smectic A and nematic phase, respectively) was extracted by data extrapolation. c) Calculated receding contact angle (using Equation 2 of the main text) of the air bubbles on an LCIPS. n = 3 for the means and standard deviations.

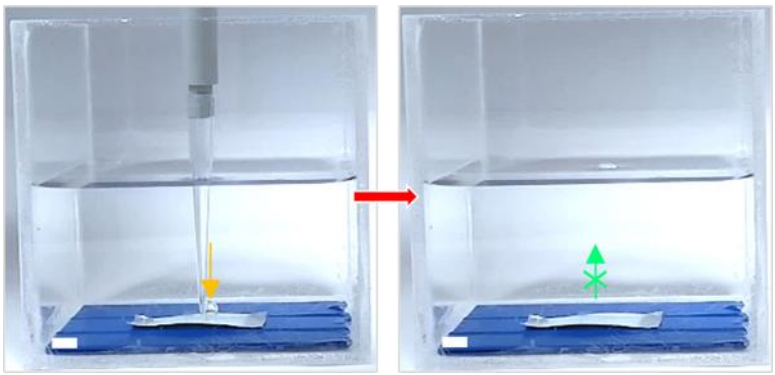

Figure S17. Release of bubble on nematic LCIPS. Photographs showing detachment of CO_2 bubble from a nematic LCIPS-coated aluminum substrate due to the weak adhesion force between the bubble and the LCIPS. The water temperature was set to 35 ^{o}C (nematic phase). Yellow arrow indicates the position of the bubble on the LCIPS. Green arrow indicates the direction of the air bubble after detaching from the LCIPS substrate, leaving it underwater. Scale bars, 5 mm.

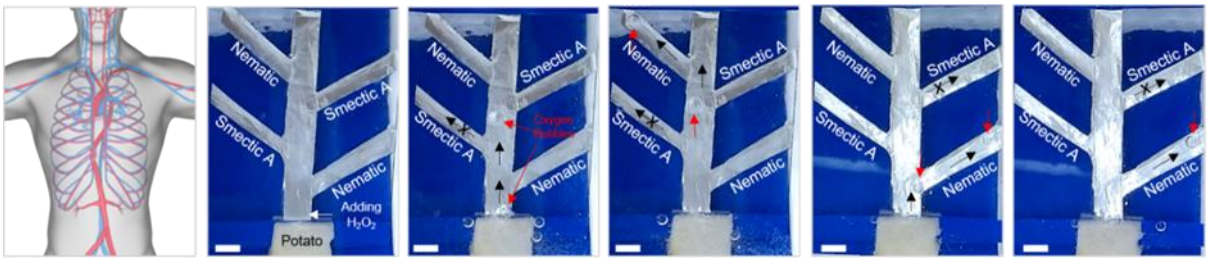

Figure S18. *In situ* generation and guided transport of oxygen bubbles on patterned LCIPS. Photographs (top view) showing the *in situ* generation of oxygen bubbles by injecting H_2O_2 onto a piece of potato attached to the LCIPS. The generated O_2 bubbles merged with each other and were transported by nematic region while remaining pinned on the smectic A region. Black dashed arrows indicate the transport of air bubbles on nematic LCIPS. Red arrows indicate the position of air bubbles. The LCIPS substrate was tilted at ~5º. Scale bars, 5 mm.

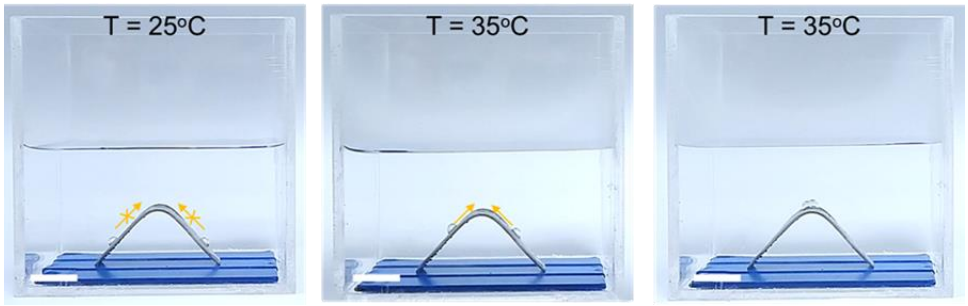

Figure S19. Heat-induced bubble sliding and merging on LCIPS. The volume of the air bubble was 10 μL. Scale bars, 5 mm.

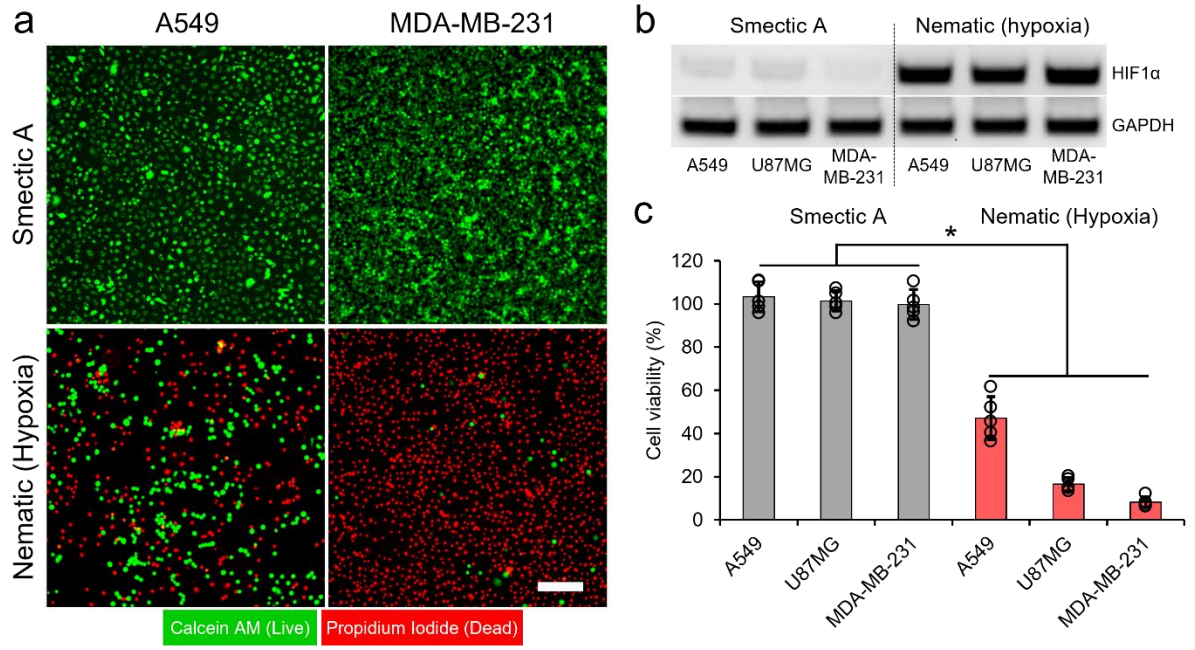

Figure S20. Manipulation of oxygen levels in cell cultures using LCIPS-based gas bubble gating system. a) Live (Calcein AM)/dead (propidium iodide) cell staining of A549 and MDA-MB-231 cells treated with 20 μg/mL of TPZ for 24 hours using different phases of LCIPS. Scale bar, 200 μm. b) RT-PCR analysis of HIF1α expression in A549 and MDA-MB-231 cells. c) Cell viability assessment of A549 and MDA-MB-231 cells treated with 20 μg/mL of TPZ for 24 hours with LCIPS in smectic A and nematic phases. Data are represented as mean standard deviation of five independent replicates ($p < 0.05$).

Supplementary Movies

Movie S1. Stimuli responsive transport of air bubbles on LCIPS. (1) In the nematic phase (25 ºC), a 10 µL gas bubble was placed on the LCIPS coated on a DMOAP functionalized glass substrate. The surface was tilted at a 5º inclination. Next, the temperature was increased to 35 ºC. (2) A 10 µL gas bubble was deposited on the LCIPS (doped with 5 wt% azobenzene) coated on a DMOAP-functionalized glass slide in the smectic A phase (25 ºC). The surface was inclined at a 10º inclination. A UV lamp with a wavelength of 365 nm was used to radiate the surface. (3) A 20 µL toluene vapor bubble was placed on a smectic A LCIPS (25 ºC) coated on a DMOAP-functionalized glass surface. The LCIPS was tilted at a 30º inclination.

Movie S2. Stability of underwater gas bubbles on a smectic A LCIPS under shaking or vibration. (1) A smectic A LCIPS was coated on a glass surface and three gas bubbles were placed on the surface. The surface was then under randomly shaking. (2) The gas bubbles were placed on a smectic A LCIPS that was randomly vibrated. The volume of each gas bubble was 10 µL.

Movie S3. Temperature regulated locomotion of LCIPS substrate. (1) Release of CO_2 bubbles on a nematic LCIPS. A nematic LCIPS coated on aluminum foil was placed in a 100 mM $NaHCO_3$ aqueous solution at 35 ºC and an HCl (1 M) solution was subsequently injected onto the LCIPS using a pipette to generate CO_2 bubbles. (2) The lifting up of the LCIPS substrate using CO_2 gas bubble generated on a smectic A LCIPS (25 ºC). (3) The tilting up of the LCIPS substrate using CO_2 gas bubble generated on a smectic A LCIPS (25 ºC). The LCIPS is lifted up when the CO_2 bubble was generated at the center. In contrast, when the CO_2 bubble was generated at the edge of LCIPS, the LCIPS is tilted up.

Movie S4. Temperature regulated bubble gating system. A gas bubble was placed on both sides of a LCIPS coated on an arc-shaped stainless-steel substrate. The volume of each gas bubble was 15 µL.

Reference

[1] T. S. Wong, S. H. Kang, S. K. Y. Tang, E. J. Smythe, B. D. Hatton, A. Grinthal, J. Aizenberg, *Nature* **2011**, *477*, 443.

[2] J. D. Smith, R. Dhiman, S. Anand, E. Reza-Garduno, R. E. Cohen, G. H. McKinley, K. K. Varanasi, *Soft Matter* **2013**, *9*, 1772.

[4] S. Anand, A. T. Paxson, R. Dhiman, J. D. Smith, K. K. Varanasi, *ACS Nano* **2012**, *6*, 10122.

[5] M. J. Kreder, D. Daniel, A. Tetreault, Z. Cao, B. Lemaire, J. V. I. Timonen, J. Aizenberg, *Phys. Rev. X* **2018**, *8*, 031053.

[6] A. Honglawan, D. A. Beller, M. C. Jr., R. D. Kamien, K. J. Stebe, S. Yang, *Proc. Natl. Acad. Sci. U.S.A.* **2013**, *110*, 34.

[7] D. K. Yoon, R. Deb, D. Chen, E. Körblova, R. Shao, K. Ishikawa, N. V. S. Rao, D. M. Walba, I. I. Smalyukh, N. A. Clark, *Proc. Natl. Acad. Sci. U.S.A.* **2010**, *107*, 21311.

[8] B. Zappone, C. Meyer, L. Bruno, E. Lacaze, *Soft Matter* **2012**, *8*, 4318.

[9] G. McHale, B. V. Orme, G. G. Wells, R. Ledesma-Aguilar, *Langmuir* **2019**, *35*, 4197.

[10] W. Xu, C. H. Choi, *Phys. Rev. Lett.* **2012**, *109*, 024504.

[11] P. S. Forsberg, C. Priest, M. Brinkmann, R. Sedev, J. Ralston, *Langmuir* **2010**, *26*, 860.

[12] G. Konvalina, H. Haick, *Acc. Chem. Res.* **2014**, *47*, 66.

[13] Z. Zhou, W. Xiong, Y. Zhang, D. Yang, T. Wang, Y. Che, J. Zhao, *Anal. Chem.* **2017**, *89*, 3814.